Effect of A-site deficiency on perovskite-type Mn^{4+}-activated $La_{5/3}MgTaO_6$ red phosphor and green luminescence of the Mn^{2+} occupied six-coordinate site in Mg_2LaTaO_6

Akihiro Nakanishi[a], Tomoya Onoe[b], Ryoto Morii[b], Kei-ichiro Murai[a,b], Toshihiro Moriga[a,b,*], Yutaka Kobayashi[c], Atsushi Sakaki[c] and Shao-Ju Shih[d]

[a] *Department of Chemical Science and Technology, Graduate School of Advanced Technology and Science, Tokushima University, 2-1 Minami-Josanjima, Tokushima 770-8506, Japan*
[b] *Department of Applied Chemistry, Graduate School of Science and Technology for Innovation, Tokushima University, 2-1 Minami-Josanjima, Tokushima 770-8506, Japan*
[c] *R&D Division, NICHIA Corporation, 491 Oka, Kaminaka, Anan, Tokushima 774-8601, Japan*
[d] *Department of Materials Science and Engineering, National Taiwan University of Science and Technology, 43 Sec. 4 Keelung Rd, Taipei 10607, Taiwan*
* Corresponding Author, (moriga@tokushima-u.ac.jp)

Abstract

White light LEDs have a long life and high energy efficiency; however, their application is limited owing to the lack of red components. Herein, we use the solid-state reaction method to fabricate a new Mn-activated perovskite-type $La_{5/3}MgTaO_6$ phosphor that exhibits red emission under UV excitation at 365 nm. A-site deficiency in the perovskite-type structure plays a crucial role in Mn^{4+} emission in $La_{5/3}MgTaO_6$ because Mn^{4+}—which is located in the non-inversion symmetry site—is activated for such an emission. In addition, the new Mn-activated pyrochlore-type Mg_2LaTaO_6 phosphor exhibited green emission under UV excitation at 254 nm owing to the oxide ion deficiency of Mg_2LaTaO_6. Based on the features of the oxide-deficient pyrochlore-type structure, we infer that Mn^{2+} may be present in the six-coordinate octahedral site with high distortion in pyrochlore-type Mg_2LaTaO_6.

Keywords: Mn-activated phosphor, perovskite, pyrochlore, octahedral distortion

1. Introduction

White LEDs are used worldwide owing to their energy efficiency, high luminous intensity, and long operational life [1–3]. These comprise blue LEDs [4] with yellow phosphors ($Y_3Al_5O_{12}:Ce^{3+}$) [5]. These colors are complementary and thus produce white light; however, white LEDs also exhibit low color rendering owing to the lack of a red component, which limits their applications [6]. Red phosphors excited by ultraviolet (UV) and blue light have been developed to solve this problem [7], and the resulting high-color-rendering white LEDs enable control of the color tone of lighting and are expected to have a wide range of applications.

Some Eu-activated red phosphors, including $CaAlSiN_3:Eu^{2+}$ and $M_2Si_5N_8:Eu^{2+}$ (M = Ca, Sr, Ba), have been synthesized for practical use [8,9]; however, Eu is expensive, and such devices are not widely available because their production is unevenly distributed around the world.

Herein, we develop Mn-activated phosphors as an alternative to Eu-activated red phosphors. Mn^{4+}-activated phosphors are known to absorb near-UV light and emit red light. Moreover, Mn is considerably cheaper than Eu [10–13]. Mn-activated phosphors have recently attracted considerable attention as promising red phosphor candidates for use in high-color-rendering white LEDs such as $NaLaMgWO_6:Mn^{4+}$ [10], $Sr_2Ca_{1-\delta}Ln_\delta WO_6:Mn^{4+}$ [11], $Sr_3LiSbO_6:Mn^{4+}$ [12], $Sr_2ScO_3F:Mn^{4+}$ [13].

Despite their potential as red phosphors, the absorption and emission of Mn^{4+} are typically assigned to forbidden transitions. Mn^{4+} preferentially occupies six-coordinate octahedral sites with a center of inversion [14]; however, a high luminescence efficiency is not achieved from the octahedral Mn^{4+} owing to its selectivity as per the Laporte rule [15]. To solve this problem, we chose $La_{5/3}MgTaO_6$ as a host material for Mn^{4+} activators. The crystal structure of $La_{5/3}MgTaO_6$ is characterized by a double perovskite-type structure with a regular deficiency of La^{3+} along the c-axis [16] (Fig. 1). $La_{5/3}MgTaO_6$ contains $[TaO_6]$ octahedra, which facilitates entry of Mn^{4+} ions into the six-coordinate octahedral sites. The Mn^{4+} in the B-site of the perovskite-type structure is thus displaced, thereby removing the center of inversion from $La_{5/3}MgTaO_6$. For example, in the defect-perovskite structures of lithium-containing lanthanum metaniobates and metatantalates, the cation at the B site is displaced toward the deficient A-site as the amount of lithium is reduced [17]. Based on these observations, we predict that the Mn^{4+}-activated $La_{5/3}MgTaO_6$ phosphor will exhibit high-intensity red emission owing to the loss of the inversion symmetry center. A Mn^{4+}-activated $SrLa_2Mg_2W_2O_{12}$ red phosphor with A-site deficiency in the structure and high luminescence was recently reported by Shi et al [18];

however, the relationship between A-site deficiency and luminescence in the perovskite-type structure has not yet been reported. Zhou et al. synthesized the perovskite-type $BaLaMgTaO_6:Mn^{4+}$ red phosphor via a high-temperature solid-state procedure [19], the final calcination temperature (1500 °C) and reaction time (6 h) of which are identical to those used in the synthesis of $La_{5/3}MgTaO_6$ [16]. In addition, the ionic radius of Ba^{2+} (1.42 Å (eight-coordination)) is similar to that of La^{3+} (1.160 Å (eight-coordination)), making Ba^{2+} a suitable dopant for La^{3+} sites [20]. In this study, we synthesized the Mn^{4+}-activated phosphors, $La_{5/3-(2/3)x}Ba_xMgTa_{0.99}O_6:0.01Mn^{4+}$ (x = 0, 0.2, 0.4, 0.6, 0.8, and 1) at 1500 °C for 6 h. By substituting Ba^{2+} into the A site of $La_{5/3}MgTaO_6$, we investigated the relationship between the A-site deficiency and the luminescence properties of the material.

We also synthesized the Mn-activated phosphors, $La_{5/3-(2/3)y}Mg_{1+y}Ta_{0.99}O_6:0.01Mn$ (y = 0, 0.2, 0.4, 0.6, 0.8, and 1), and investigated the effect of increasing y on their crystal structure evolution and luminescence properties. With a y value of 1, the chemical composition of this phosphor is represented as Mg_2LaTaO_6, which has an oxide ion-deficient pyrochlore-type structure [21]. Mn^{4+}-activated pyrochlore-type $RE_2Sn_2O_7$ ($RE^{3+} = Y^{3+}$, Lu^{3+} or Gd^{3+}) phosphors were previously shown to exhibit red luminescence [22]. To the best of our knowledge, all Mn-activated pyrochlore-type phosphors emit red light. Inspired by this, we synthesized the first Mn-activated pyrochlore-type Mg_2LaTaO_6 phosphor.

2. Materials and methods

2.1 Sample synthesis

$La_{5/3-(2/3)x}Ba_xMgTa_{0.99}Mn_{0.01}O_6$ (x = 0, 0.2, 0.4, 0.6, 0.8, and 1) and $La_{5/3-(2/3)y}Mg_{1+y}Ta_{0.99}Mn_{0.01}O_6$ (y = 0, 0.2, 0.4, 0.6, 0.8, and 1) phosphors were synthesized by a solid-state reaction. The Mn doping level was fixed at 1% of Ta. Stoichiometric amounts of La_2O_3 (99.9%, Kojundo Chemical, Japan), $4MgCO_3{\cdot}Mg(OH)_2{\cdot}5H_2O$ (485.65 g/mol, Kishida Chemical, Japan), Ta_2O_5 (99.95%, Kanto Chemical, Japan), $MnCO_3$ (99.9%, Kojundo Chemical, Japan), and $BaCO_3$ (99.9%, Kanto Chemical, Japan) were ground and mixed in an agate mortar for 40 min. After calcination at 1200 °C for 4 h, the mixture was cooled to room temperature and thereafter mixed for a further 20 min. Finally, the mixture was calcined at 1500 °C for 6 h to obtain the desired products.

2.2 Characterization

The crystalline structures of the phosphors were investigated at room temperature

using powder X-ray diffraction (XRD, SmartLab X-ray Diffractometer, Rigaku, Japan) with Cu-Kα radiation at 45 kV, 200 mA, and 2θ in the range of 10–60°. The particle shape and size were determined by scanning electron microscopy (SEM, JSM-6510A, JEOL, Japan). The luminescence properties of all the phosphors were measured by fluorescence spectrometry (FP-8300 Spectrofluorometer, JASCO, Japan). The same amounts of phosphors (weighted 0.150 g) were used to compare with the same holder. The X-ray absorption near edge structure (XANES) spectrum of the Mn-K edge in fluorescent mode was measured using the BI16B2 beamline at SPring-8, Japan. X-ray energy selection was achieved using a silicon (111) double crystal monochromator. A 25-element solid-state detector (25-element SSD) was used owing to the low concentration of Mn. A Cr metal foil was set in front of the SSD for band-pass filter. The XANES spectra were measured at a rate of 45 (x, y = 1 samples) and 54 (x = 0 sample) seconds per point, respectively. After the XANES measurement, the background process was conducted by REX2000 software.

3. Results and Discussion

3.1 $La_{5/3-(2/3)x}Ba_xMgTa_{0.99}Mn_{0.01}O_6$ (x = 0, 0.2, 0.4, 0.6, 0.8, and 1) phosphors

The XRD patterns of $La_{5/3-(2/3)x}Ba_xMgTa_{0.99}Mn_{0.01}O_6$ (x = 0, 0.2, 0.4, 0.6, 0.8, and 1) phosphors calcined at 1500 °C for 6 h are shown in Fig. 2. The diffraction patterns of the samples with x = 0 and 1 are consistent with the Joint Committee on Powder Diffraction Standards (JCPDS) card peak patterns of $La_{5/3}MgTaO_6$ [16] and $BaLaMgTaO_6$ [23], respectively, confirming the formation of single phase phosphors. The patterns of samples with x = 0.2–0.8 did not exhibit any peaks corresponding to other phases. The peak at ~32° continuously shifted to a lower angle with increasing x, indicating that Ba was successfully doped into the perovskite-type structure (Fig. 2, right hand side).

SEM images of Mn^{4+}-activated $La_{5/3}MgTaO_6$ (x = 0) and $BaLaMgTaO_6$ (x = 1) phosphors are shown in Fig. 3(a) and (b), respectively. We observed coarse particles measuring ~10–20 micrometers and fine particles measuring several micrometers.

The excitation and emission spectra of $La_{5/3-(2/3)x}Ba_xMgTa_{0.99}Mn_{0.01}O_6$ (x = 0, 0.2, 0.4, 0.6, 0.8, and 1) phosphors are shown in Fig. 4(a) and Fig. 4(b), respectively. The excitation spectra showed an absorption maximum at ~365 nm, while the fluorescence spectra showed red emission with a maximum at ~706 nm. The sample with x = 0 exhibited the strongest absorption of UV light and emission of red light at ~365 and 706 nm, respectively, demonstrating its potential as a phosphor for high-color-rendering

white LEDs by applying near-UV light excitation. As the amount of Ba^{2+} substitution increased, both the absorption and emission intensities tended to decrease.

Images of $La_{5/3-(2/3)x}Ba_xMgTa_{0.99}Mn_{0.01}O_6$ (x = 0, 0.2, 0.4, 0.6, 0.8, and 1) phosphors under UV excitation of 365 nm (Fig. 5) show that the red luminescence tends to be quenched with increasing x. The sample with x = 0 exhibited the strongest red emission. We hypothesize that the center of inversion in $La_{5/3}MgTaO_6$, was lost owing to the displacement of Mn^{4+} occupying the B-site toward the deficient A-site to avoid electrostatic repulsion. Accordingly, the forbidden transition was relaxed in the x = 0 sample. In addition, the luminescence tended to be increasingly quenched with increasing x, indicating that reducing the A-site deficiency by the substitution of Ba^{2+} revives the center of inversion (Fig. 6).

XANES is an effective technique to probe the local coordination environment at a particular location in the structure. Yamamoto introduced the importance of the intensity of the pre-edge peak in terms of the d-p hybridization, which is dominated by the orbital symmetry and can be explained by group theory. The formation of the d-p hybridized orbital results in an intense pre-edge peak owing to the mixing of s-p electric dipole transitions [24]. Farges reported that the intensity of the pre-edge peak at ~6540 eV in the Mn K-edge XANES spectrum increased as the symmetry around the Mn^{2+} center was reduced [25].

The Mn K-edge XANES spectra of $La_{5/3}MgTa_{0.99}Mn_{0.01}O_6$ (x = 0) and $BaLaMgTa_{0.99}Mn_{0.01}O_6$ (x = 1) phosphors are shown in Fig. 7. A low-intensity pre-edge peak was observed at approximately 6540–6545 eV in A-site deficient perovskite-type structure. Therefore, this result provides evidence that Mn^{4+} occupies the non-inversion center and explains the strong red emission of the A-site deficient perovskite-type structure.

3.2 $La_{5/3-(2/3)y}Mg_{1+y}Ta_{0.99}Mn_{0.01}O_6$ (y = 0, 0.2, 0.4, 0.6, 0.8, and 1) phosphors

The XRD patterns of the $La_{5/3-(2/3)y}Mg_{1+y}Ta_{0.99}Mn_{0.01}O_6$ (y = 0, 0.2, 0.4, 0.6, 0.8, and 1) phosphors calcined at 1500 °C for 6 h are shown in Fig. 8. The pattern of the sample with y = 0 matched the peak pattern of $La_{5/3}MgTaO_6$, confirming the single phase phosphor. In contrast, a new diffraction peak appeared at ~29° as y increased. These star-shaped peaks are derived from the oxide ion-deficient pyrochlore-type structure of Mg_2LaTaO_6 [21]. A small amount of MgO was also detected as a byproduct in samples with y = 0.2–1. Magnification of the strongest diffraction peaks at ~27°–33° shows that the peak shift was not significant, with an increase in y, the intensity of the peaks derived from $La_{5/3}MgTaO_6$ decreased and that derived from Mg_2LaTaO_6 increased.

This result demonstrates that the addition of Mg to La does not form a solid solution in the perovskite-type $La_{5/3}MgTaO_6$ structure.

The perovskite-type structure was retained in $La_{5/3-(2/3)x}Ba_xMgTa_{0.99}Mn_{0.01}O_6$ (x = 0, 0.2, 0.4, 0.6, 0.8, and 1) regardless of the x value; however, $La_{5/3-(2/3)y}Mg_{1+y}Ta_{0.99}Mn_{0.01}O_6$ (y = 0, 0.2, 0.4, 0.6, 0.8, and 1) formed a pyrochlore-type structure as y increased. This result was attributed to the difference in the ionic radii of Mg^{2+} and Ba^{2+} used as dopants. Because the ionic radius of Ba^{2+} (1.42 Å (eight-coordination)) is larger than that of Mg^{2+} (0.89 Å (eight-coordination)) [20], the perovskite-type structure, wherein the A-site cation prefers a greater coordination number, is stabilized in the $La_{5/3-(2/3)x}Ba_xMgTa_{0.99}Mn_{0.01}O_6$ (x = 0, 0.2, 0.4, 0.6, 0.8, and 1) system.

An SEM image of the Mn-activated Mg_2LaTaO_6 (y = 1) phosphor is shown in Fig. 9. The particle size of this phosphor was several micrometers, and the particles were smoother and more uniform than those of the Mn^{4+}-activated perovskite-type phosphors.

The emission spectra of $La_{5/3-(2/3)y}Mg_{1+y}Ta_{0.99}Mn_{0.01}O_6$ (y = 0, 0.2, 0.4, 0.6, and 0.8) phosphors excited at 365 nm are shown in Fig. 10. As y increased, the emission intensity tended to decrease.

Images of $La_{5/3-(2/3)y}Mg_{1+y}Ta_{0.99}Mn_{0.01}O_6$ (y = 0, 0.2, 0.4, 0.6, 0.8, and 1) phosphors under UV excitation at 365 nm are shown in Fig. 11. The quenching of red luminescence tends to increase with increasing y. The XRD patterns revealed that the extent of the $La_{5/3}MgTaO_6$ phase decreased with increasing y value (Fig. 8); therefore, the decreasing trend in the emission intensity is caused by a reduction in the amount of the $La_{5/3}MgTaO_6$ phase that emits red light.

The excitation spectra of $La_{5/3-(2/3)y}Mg_{1+y}Ta_{0.99}Mn_{0.01}O_6$ (y = 0.2, 0.4, 0.6, 0.8, and 1) phosphors at 540 nm showed absorption maxima at ~254 nm (Fig. 12(a)), while the fluorescence emission spectrum showed green emission with a maximum at ~540 nm (Fig. 12(b)). The intensity of this green emission increased as y increased, suggesting that the amount of the pyrochlore-type Mg_2LaTaO_6 phase, which emits green light, increases with increasing y, whereas the amount of the perovskite-type $La_{5/3}MgTaO_6$ phase, which emits red light, decreases.

Images of $La_{5/3-(2/3)y}Mg_{1+y}Ta_{0.99}Mn_{0.01}O_6$ (y = 0, 0.2, 0.4, 0.6, 0.8, and 1) phosphors under UV 254 nm are shown in Fig. 13. The sample with y = 0 consisted of a single phase of $La_{5/3}MgTaO_6$: thus, the red luminescence must be derived from the perovskite-type $La_{5/3}MgTaO_6$. In contrast, the sample with y = 1 primarily contained the Mg_2LaTaO_6 phase, demonstrating that the green luminescence was derived from the

pyrochlore-type Mg_2LaTaO_6. Orange/yellow emissions were observed from samples with $y = 0.4$ and 0.6 owing to the mixture of the perovskite-type red phosphor and pyrochlore-type green phosphor in the samples with $y = 0.2$ to 0.8.

The local coordination environment of pyrochlore-type Mg_2LaTaO_6 was explored, and a schematic of its structure was produced (Fig. 14). The composition of the ideal pyrochlore-type structure is expressed as $A_2B_2X_7$, in which the A-cation occupies the 16d site (eight-coordinate site), and the B-cation occupies the 16c site (six-coordinate site) [26]. The X anions occupy the 48f and 8b sites, while the 8a site is unoccupied. Kumar et al. [21] found that Mg and La were randomly distributed across the 16d sites (A-site) in oxide-ion deficient pyrochlore-type Mg_2LaTaO_6, while Mg and Ta were randomly distributed across the 16c sites (B-site). The sum of the bond strengths of the 48f sites and 8b sites in Mg_2LaTaO_6 is calculated by Pauling's second law [27], as shown in Fig. 15. The sum of the bond strengths of the 48f position is closer to -2 than that of the 8b position, suggesting that oxide ions are preferentially lost from the 8b. Accordingly, this deficient pyrochlore-type Mg_2LaTaO_6 structure consists of AO_6 and BO_6 octahedra owing to the empty 8b sites. Both AO_6 and BO_6 octahedra have a center of inversion identical to that of the nominal pyrochlore-type structure. Ramesha et al. reported an oxygen ion-deficient pyrochlore-type Pb_2MnReO_6 [28]. Their refinement demonstrated that Mn^{2+} and Re^{6+} are disordered at 16c sites, while the O^{2-} anions occupied the 48f sites and the 8b site was unoccupied. The crystal structure of Pb_2MnReO_6 is shown in Fig. 16. The BO_6 polyhedra in Pb_2MnReO_6 were highly distorted in a similar way to the highly distorted BO_6 octahedron found in Mg_2LaTaO_6 [21].

The coordination environment in the vicinity of Mn was evaluated using XANES. The Mn K-edge XANES spectrum of $Mg_2LaTa_{0.99}Mn_{0.01}O_6$ ($y = 1$) phosphor is shown in Fig. 17. The pre-edge peak was not identified in the spectrum of the pyrochlore-type Mg_2LaTaO_6 phosphor, leading us to conclude that Mn occupied the site with a center of inversion.

Mn^{4+} phosphors emit red light regardless of the parent material [10–13]; however, the emission wavelength of Mn^{2+}-activated phosphors is dependent on the crystal field. As the crystal field becomes stronger, the emission wavelength shifts toward longer wavelengths. For example, in the case of the oxide phosphor, Mn^{2+} in a four-coordinate site without a center of inversion exhibits green emission owing to the relatively weak crystal field, while that in a six-coordinate site emits orange/red light as a result of the stronger crystal field [30–33].

Table 1 shows the emission wavelengths and coordination numbers of the Mn^{2+} oxide

phosphors [30–40]. The Mn-activated Mg_2LaTaO_6 phosphors in which six-coordinate sites are occupied exhibited an emission peak at an intermediate wavelength (540 nm), suggesting that the highly distorted BO_6 octahedron may weaken the crystal field, thus resulting in green emission from Mn^{2+}.

4. Conclusion

Cost-effective red-emitting phosphors with structures of $La_{5/3-(2/3)x}Ba_xMgTa_{0.99}Mn_{0.01}O_6$ (x = 0, 0.2, 0.4, 0.6, 0.8, and 1) and $La_{5/3-(2/3)y}Mg_{1+y}Ta_{0.99}Mn_{0.01}O_6$ (y = 0, 0.2, 0.4, 0.6, 0.8, and 1) were synthesized by solid-state reaction for use in high-color-rendering white LEDs. An investigation of the luminescence properties of Mn-activated $La_{5/3-(2/3)x}Ba_xMgTa_{0.99}Mn_{0.01}O_6$ (x = 0, 0.2, 0.4, 0.6, 0.8, and 1) phosphors suggests that the absorption and emission of Mn^{4+} in perovskite-type $La_{5/3}MgTaO_6$ is related to the A-site deficiency of the structure. The deficiency of La^{3+} in $La_{5/3}MgTaO_6$ causes Mn^{4+} to occupy distorted six-coordinate octahedral sites, thereby relaxing the forbidden transition. The XANES spectra showed evidence that Mn^{4+} was located at the non-inversion center in the A-site deficient perovskite-type structure. The Mn^{4+}-activated $La_{5/3}MgTaO_6$ phosphor exhibits red emission under UV excitation at 365 nm, and thus has potential applications as a red phosphor in high-color-rendering white LEDs. Similarly, the pyrochlore-type Mg_2LaTaO_6 phosphor exhibited green emission at ~540 nm under UV excitation at 254 nm. In conjunction with the crystallographic data of Mg_2LaTaO_6, this result suggests that Mn^{2+} is present in the six-coordinated octahedral sites with a center of inversion in Mg_2LaTaO_6. Our results suggest that the highly distorted BO_6 octahedron may weaken the crystal field, thereby resulting in green emission, and explaining the fact that Mn-activated Mg_2LaTaO_6 phosphor exhibited green emission despite the occupation of the six-coordinate sites.

Acknowledgements

This research was partially supported by the Ministry of Education, Science, Sports, and Culture, Grant-in Aid for Scientific Research (B), 2018–2022 (18H02059, Toshihiro Moriga). The Mn-K XANES measurements were performed with the approval of the Japan Synchrotron Radiation Research Institute (JASRI) (Proposal No. 2022A5380).

Declaration of competing interest

We declare that we do not have persons with conflict of interest.

References

[1] E.F. Schubert, J.K. Kim, Solid-state light sources getting smart, Science 308 (2005) 1274–1278. DOI: 10.1126/science.1108712.

[2] C.J. Humphreys, Solid-state lighting, MRS Bull. 33 (2008) 459–470. DOI: 10.1557/mrs2008.91.

[3] C.C. Lin, R.S. Liu, Advances in phosphors for light-emitting diodes, J. Phys. Chem. Lett. 2 (2011) 1268–1277. DOI: 10.1021/jz2002452.

[4] S. Nakamura, T. Mukai, M. Senoh, Candela-class high-brightness InGaN/AlGaN double-heterostructure blue-light-emitting diodes, Appl. Phys. Lett. 64 (1994) 1687–1689. DOI: 10.1063/1.111832.

[5] Z. Xia, A. Meijerink, Ce^{3+}-Doped garnet phosphors: composition modification, luminescence properties and applications, Chem. Soc. Rev. 46 (2017) 275–299. DOI: 10.1039/c6cs00551a.

[6] Z. Xia, Q. Liu, Progress in discovery and structural design of color conversion phosphors for LEDs, Prog. Mater. Sci. 84 (2016) 59–117. DOI:10.1016/j.pmatsci.2016.09.007

[7] Y. Zhang, L. Luo, Guantong Chen, Y. Liu, R. Liu, X. Chen, Green and red phosphor for LED backlight in wide color gamut LCD, J. Rare Earths 38 (2020) 1–12. DOI: 10.1016/j.jre.2019.10.005.

[8] K. Uheda, N. Hirosaki, H. Yamamoto, Host lattice materials in the system Ca_3N_2 -AlN-Si_3N_4 for white light emitting diode, Phys. Stat. Sol. (A) 203 (2006) 2712–2717. DOI: 10.1002/pssa.200669576.

[9] Y.Q. Li, J.E.J. van Steen, J.W.H. van Krevel, G. Botty, A.C.A. Delsing, F.J. DiSalvo, G. de With, H.T. Hintzen, Luminescence properties of red-emitting $M_2Si_5N_8:Eu^{2+}$ (M = Ca, Sr, Ba) LED conversion phosphors, J. Alloys Compd. 417 (2006) 273–279. DOI: 10.1016/j.jallcom.2005.09.041.

[10] X. Huang, J. Liang, B. Li, L. Sun, J. Lin, High-efficiency and thermally stable far-red-emitting $NaLaMgWO_6:Mn^{4+}$ phosphors for indoor plant growth light-emitting diodes, Opt. Lett. 43 (2018) 3305–3308. DOI: 10.1364/OL.43.003305.

[11] K. Li, J. Du, D. Poelman, H. Vrielinck, D. Mara, R. Van Deun, Achieving efficient red-emitting $Sr_2Ca_{1-\delta}Ln\delta WO_6:Mn^{4+}$ (Ln = La, Gd, Y, Lu, δ = 0.10) Phosphors with extraordinary luminescence thermal stability for potential UV-LEDs application

via facile ion substitution in luminescence-ignorable $Sr_2CaWO_6:Mn^{4+}$, ACS Mater. Lett. 2 (2020) 771–778. DOI: 10.1021/acsmaterialslett.0c00212.
[12] L. Fu, Y. Yang, Y. Zhang, X. Ren, Y. Zhu, J. Zhu, Y. Wu, J. Wang, X. Feng, The novel $Sr_3LiSbO_6:Mn^{4+}$, Ca^{2+} far-red-emitting phosphors with over 95% internal quantum efficiency for indoor plant growth LEDs, J. Lumin. 237 (2021) 118165.
[13] H. Kato, Y. Takeda, M. Kobayashi, H. Kobayashi, M. Kakihana, Photoluminescence properties of layered perovskite-type strontium scandium oxyfluoride activated with Mn^{4+}, Front. Chem. 6 (2018) 467. DOI: 10.3389/fchem.2018.00467.
[14] D. Chen, Y. Zhou, Jiasong Zhong, A review on Mn^{4+} activators in solids for warm white light-emitting diodes, RSC Adv. 6 (2016) 86285–86296. DOI: 10.1039/C6RA19584A.
[15] O. Laporte, W.F. Meggers, Some rules of spectral structure, J. Opt. Soc. Am. 11 (1925) 459–463. DOI: 10.1364/JOSA.11.000459.
[16] D.D. Khalyavin, A.M.R. Senos, P.Q. Mantas, D.N. Argyriou, I. Tarroso Gomes, L.G. Vieira, J.L. Ribeiro, Structure and dielectric characterization of a new A-site deficient $La_{5/3}MgTaO_6$ perovskite, J. Solid State Chem. 180 (2007) 41–48. DOI: 10.1016/j.jssc.2006.09.016.
[17] A. Belous, E. Pashkova, O. Gavrilenko, O. V'yunov, L. Kovalenko, Solid electrolytes based on lithium-containing lanthanum metaniobates and metatantalates with defect-perovskite structure, Ionics 9 (2003) 21–27. DOI: 10.1007/BF02376532.
[18] L. Shi, Y. Han, S. Wang, J. Jiao, S. Chang, Z. Mu, Z. Mao, D. Wang, Z. Zhang, X. Lu, Synthesis and photoluminescence properties of high thermal stability Mn^{4+} in orthorhombic $SrLa_2Mg_2W_2O_{12}$ red phosphor for warm w-LEDs, J. Mater. Sci.: Mater. Electron. 31 (2020) 4677–4686. DOI: 10.1007/s10854-020-03022-5
[19] C. Zhou, Y. Zhang, J. Zhu, X. Ren, Y. Zhu, P. Yin, L. Zhao, J. Wang, X. Feng, Enhanced luminescence performances of $BaLaMgTaO_6:Mn^{4+}$ red phosphor by Bi^{3+}, Ca^{2+} doping for indoor plant lighting supplementary LED, Spectrochim. Acta, Part A 268 (2022) 120655. DOI:10.1016/j.saa.2021.120655
[20] R.D. Shannon, Revised effective ionic radii and systematic studies of interatomic distances in halides and chalcogenides, Acta Cryst. A 32 (1976) 751–767. DOI: 10.1107/S0567739476001551.
[21] S. Senthil Kumar, K.V.O. Nair, J. James, Mg_2MTaO_6 (M = Nd or La): a group of new pyrochlore oxides, J. Solid State Chem. 177 (2004) 3873–3878. DOI: 10.1016/j.jssc.2004.07.033.
[22] T. Senden, F. T.H. Broers, A. Meijerink, Comparative study of the Mn^{4+} $^2E \rightarrow$

$^4A_2$ luminescence in isostructural $RE_2Sn_2O_7:Mn^{4+}$ pyrochlores ($RE^{3+} = Y^{3+}$, Lu^{3+} or Gd^{3+}), Opt. Mater. 60 (2016) 431-437. DOI: 10.1016/j.optmat.2016.08.024

[23] Y.-I. Kim, P.M. Woodward, Crystal structures and dielectric properties of ordered double perovskites containing Mg^{2+} and Ta^{5+}, J. Solid State Chem. 180 (2007) 2798–2807. DOI: 10.1016/j.jssc.2007.08.003.

[24] T. Yamamoto, Assignment of pre-edge peaks in K-edge x-ray absorption spectra of 3d transition metal compounds: electric dipole or quadrupole?, X-ray Spectrom. 37 (2008) 572-584. DOI: 10.1002/xrs.1103

[25] F. Farges, Ab initio and experimental pre-edge investigations of the Mn K-edge XANES in oxide-type materials, Phys. Rev. B. 71 (2005) 155109. DOI: 10.1103/PhysRevB.71.155109

[26] A. Jerez, M.L. Lopez, S. Garcia-Martin, M.L. Veiga, C. Pico, Defect pyrochlore structure $A_2B_2X_6$: A general approach to the coordination polyhedra around the metal ions, J. Mater. Sci. 26 (1991) 5163–5166. DOI: 10.1007/BF01143208.

[27] L. Pauling, The principles determining the structure of complex ionic crystals, J. Am. Chem. Soc. 51 (1929) 1010–1026. DOI: 10.1021/ja01379a006.

[28] K. Ramesha, L. Sebastian, B. Eichhorn, J. Gopalakrishnan, Perovskite and pyrochlore modifications of Pb_2MnReO_6: synthesis, structure, and electronic properties, Chem. Mater. 15 (2003) 668–674. DOI: 10.1021/cm0207494.

[29] K. Momma, F. Izumi, VESTA 3 for three-dimensional visualization of crystal, volumetric and morphology data, J. Appl. Crystallogr. 44 (2011) 1272–1276. DOI: 10.1107/S0021889811038970.

[30] K.W. Park, H.S. Lim, S.W. Park, G. Deressa, J.S. Kim, Strong blue absorption of green $Zn_2SiO_4:Mn^{2+}$ phosphor by doping heavy Mn^{2+} concentrations, Chem. Phys. Lett. 636 (2015) 141–145. DOI: 10.1016/j.cplett.2015.07.032.

[31] Y. Wei, X. Han, E. Song, Q. Zhang, Photoluminescence and phosphorescence of Mn^{2+} ion activated green phosphor $Na_2ZnSiO_4:Mn^{2+}$ synthesized by self-reduction, Mater. Res. Bull. 113 (2019) 90–96. DOI: 10.1016/j.materresbull.2019.01.022.

[32] L. Wu, B. Wang, Y. Zhang, L. Li, H.R. Wang, H. Yi, Y.F. Kong, J.J. Xu, Structure and photoluminescence properties of a rare-earth free red-emitting $Mn^{(2+)}$-activated $KMgBO_3$, Dalton Trans. 43 (2014) 13845–13851. DOI: 10.1039/c4dt01524j.

[33] L.T.T. Vien, N. Tu, D.X. Viet, D.D. Anh, D.H. Nguyen, P.T. Huy, Mn^{2+}- doped Zn_2SnO_4 green phosphor for WLED applications, J. Lumin. 227 (2020) 117522. DOI: 10.1016/j.jlumin.2020.117522

[34] W. Ran, L. Wang, Q. Liu, G. Liu, D. Qu, X. Pan, J. Shi, Mn^{2+} doped $CdAl_2O_4$ phosphors with new structure and special fluorescence properties: experimental and

theoretical analysis, RSC Adv. (2017) 17612–17619. https://doi.org/10.1039/C7RA01623A

[35] L. Hu, Q. Wang, X. Wang, Y. Li, Y. Wang, X. Peng, Photoluminescence and cathodoluminescence properties of $Na_2MgGeO_4:Mn^{2+}$ green phosphors, RSC Adv. 5 (2015) 104708–104714. DOI: 10.1039/c5ra18558k.

[36] X. Ding, G. Zhu, Q. Wang, Y. Wang, Rare-earth free narrow-band green-emitting $KAlSi_2O_6:Mn^{2+}$ phosphor excited by blue light for LED-phosphor material, the RSC Adv. 5 (2015) 30001–30004. DOI: 10.1039/c5ra03323c.

[37] B. Lei, Y. Liu, Z. Ye, C. Shi, Luminescence properties of $CdSiO_3:Mn^{2+}$ phosphor, J. Lumin. 109 (2004) 215–219. DOI: 10.1016/S0022-2313(04)00147-4.

[38] G. Doke, A. Antuzevics, G. Krieke, A. Kalnina, M. Springis, A. Sarakovskis, UV and X-ray excited red persistent luminescence in Mn^{2+} doped $MgGeO_3$ material synthesized in air and reducing atmosphere, J. Lumin. 234 (2021) 117995. DOI: 10.1016/j.jlumin.2021.117995.

[39] W. Gong, J. Luo, W. Zhou, J. Fan, Z. Sun, S. Zeng, H. Pan, Z. Zhu, X. Yang, Z. Yu, X. Zhang, Thermal-stable blue-red dual-emitting $Na_2Mg_2Si_6O_{15}$: Eu^{2+}, Mn^{2+} phosphor for plant growth lighting, J. Lumin. 239 (2021) 118372. DOI: 10.1016/j.jlumin.2021.118372.

[40] B. Wang, Y. Kong, Z. Chen, X. Li, S. Wang, Q. Zeng, Thermal stability and photoluminescence of Mn^{2+} activated green-emitting feldspar phosphor $SrAl_2Si_2O_8$: Mn^{2+} for wide gamut w-LED backlight, Opt. Mater. 99 (2020) 109535. DOI: 10.1016/j.optmat.2019.109535.

Figure and Table Captions

Fig. 1 Crystal structure of $La_{5/3}MgTaO_6$. La^{3+} in the center is missing. Mg^{2+} and Ta^{5+} ions may be shifted along the respective arrows.

Fig. 2 XRD patterns of $La_{5/3-(2/3)x}Ba_xMgTa_{0.99}O_6$:0.01$Mn^{4+}$ (x = 0, 0.2, 0.4, 0.6, 0.8, and 1).

Fig. 3 SEM images of Mn^{4+}-activated (a) $La_{5/3}MgTaO_6$ (x = 0) and (b) $BaLaMgTaO_6$ (x = 1) phosphors.

Fig. 4 (a) Excitation and (b) emission spectra of $La_{5/3-(2/3)x}Ba_xMgTa_{0.99}O_6$:0.01$Mn^{4+}$ (x = 0, 0.2, 0.4, 0.6, 0.8, and 1).

Fig. 5 Photographs of $La_{5/3-(2/3)x}Ba_xMgTa_{0.99}O_6$:0.01$Mn^{4+}$ (x = 0, 0.2, 0.4, 0.6, 0.8, and 1) under UV excitation at 365 nm.

Fig. 6 Crystal structure of $La_{5/3}MgTaO_6$ (left) and $BaLaMgTaO_6$ (right). The A-site cation deficiency in $La_{5/3}MgTaO_6$ decreases with increasing x. The B-site cation is displaced in the direction of A-site deficiency to avoid electrostatic repulsion with the A-site cation La^{3+}.

Fig. 7 Mn K edge normalized XANES spectra of $La_{5/3}MgTa_{0.99}Mn_{0.01}O_6$ and $BaLaMgTa_{0.99}Mn_{0.01}O_6$ phosphors.

Fig. 8 XRD patterns of $La_{5/3-(2/3)y}Mg_{1+y}Ta_{0.99}O_6$:0.01Mn ($y$ = 0, 0.2, 0.4, 0.6, 0.8, and 1).

Fig. 9 SEM image of Mn-activated Mg_2LaTaO_6 (y = 1) phosphor.

Fig. 10 Emission spectra of $La_{5/3-(2/3)y}Mg_{1+y}Ta_{0.99}O_6$:0.01Mn ($y$ = 0, 0.2, 0.4, 0.6, and 0.8).

Fig. 11 Photos of $La_{5/3-(2/3)y}Mg_{1+y}Ta_{0.99}O_6$:0.01Mn ($y$ = 0, 0.2, 0.4, 0.6, 0.8, and 1) under UV excitation at 365 nm.

Fig. 12 (a) Excitation and (b) emission spectra of $La_{5/3-(2/3)x}Mg_{1+y}Ta_{0.99}O_6$:0.01$Mn^{2+}$ (x = 0, 0.2, 0.4, 0.6, 0.8, and 1).

Fig. 13 Photos of $La_{5/3-(2/3)y}Mg_{1+y}Ta_{0.99}O_6$:0.01Mn ($y$ = 0, 0.2, 0.4, 0.6, 0.8, and 1) under UV excitation at 254 nm.

Fig. 14 Schematic of pyrochlore-type structure. A and B cations occupy the 16d site (eight-coordinate site) and 16c site (six-coordinate site), respectively. X anions occupy the 48f and 8b sites, while the 8a site is unoccupied.

Fig. 15 Sum of the bond strengths of 48f and 8b site in Mg_2LaTaO_6. It is defined by the following equation: $-\sum_i \frac{V_i}{n_i}$, where V_i and n_i are the valence and coordination number of cation, respectively.

Fig. 16 Crystal structure of Pb_2MnReO_6 drawn using VESTA [29]. The BO_6 octahedron is highly distorted. The purple, black, and red spheres represent Mn/Re, Pb, and

O, respectively. Mn^{2+} and Re^{6+} are disordered at 16c sites (purple polyhedral site).

Fig. 17 Mn K edge normalized XANES spectra of $Mg_2LaTa_{0.99}Mn_{0.01}O_6$ phosphors.

Table 1 Emission wavelength and coordination number of Mn^{2+}-activated oxide phosphors.

Abstract

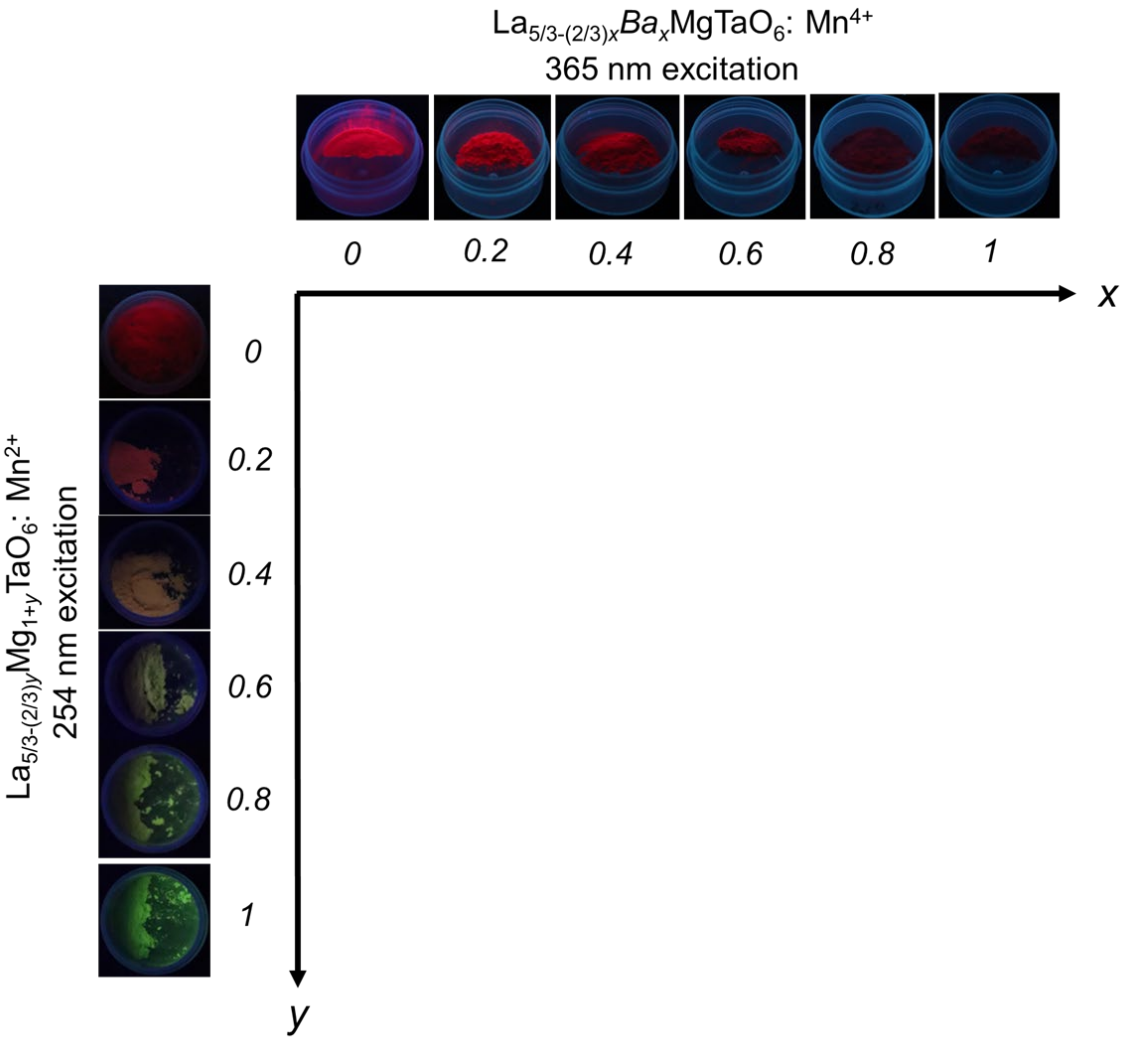
La5/3-(2/3)xBaxMgTaO6: Mn4+
365 nm excitation
0
0.2
0.4
0.6
0.8
1
x
La5/3-(2/3)yMg1+yTaO6: Mn2+
254 nm excitation
0
0.2
0.4
0.6
0.8
1
y

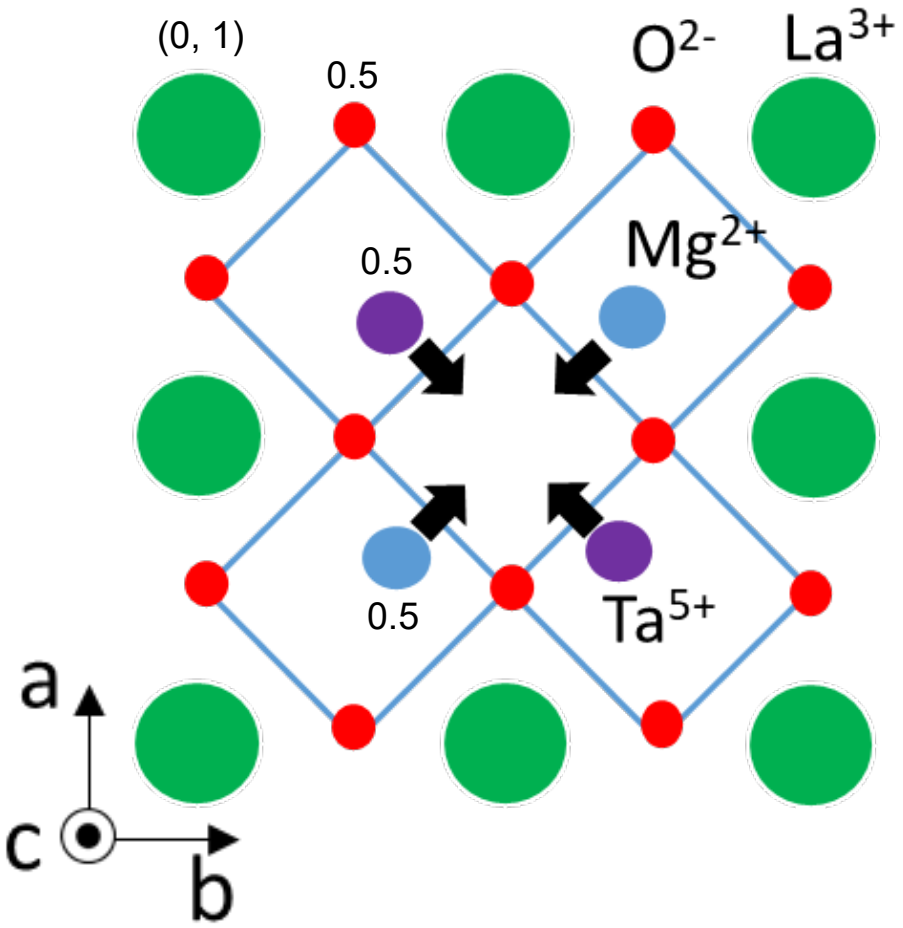

Fig. 1

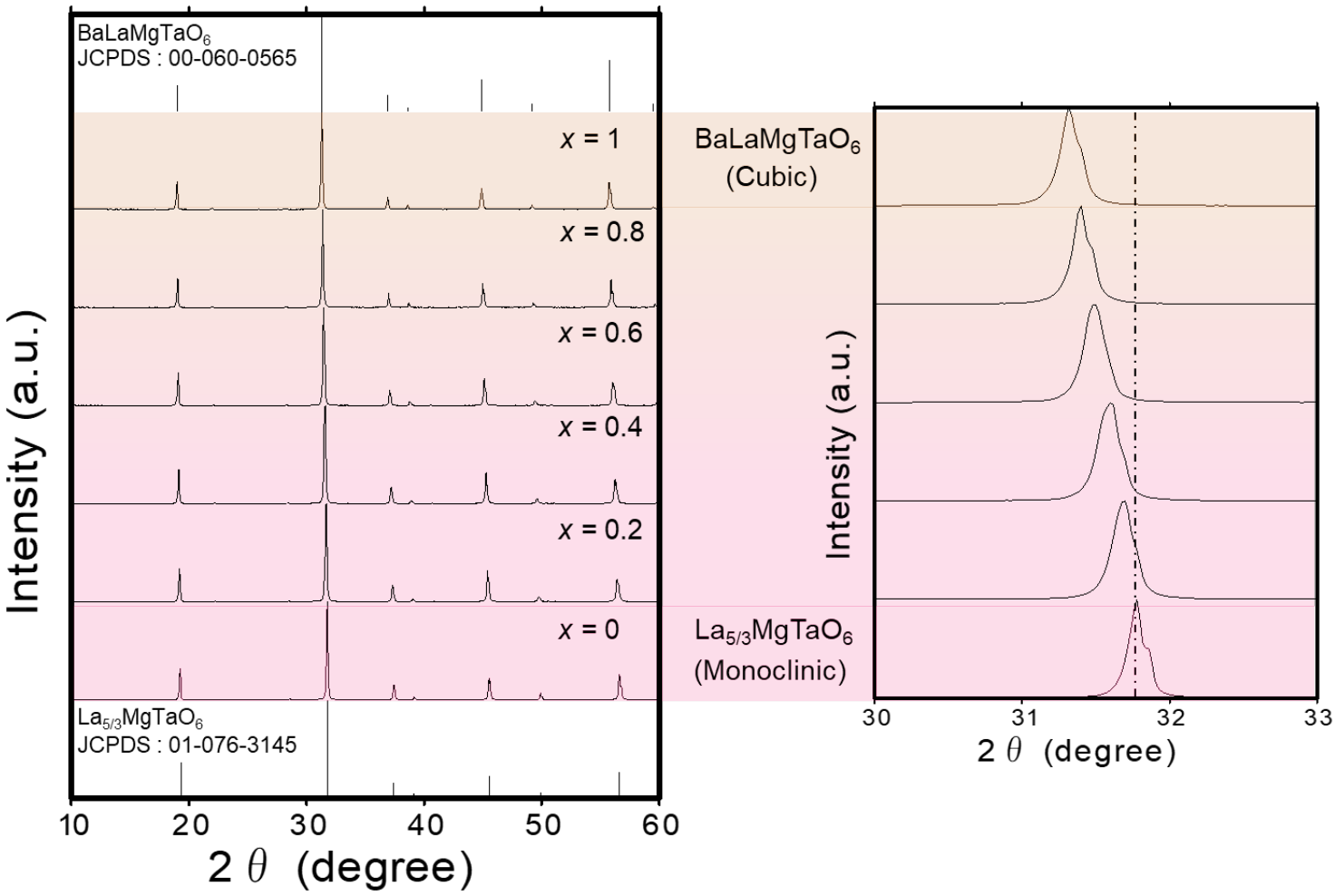
BaLaMgTaO6
JCPDS : 00-060-0565
x = 1
x = 0.8
x = 0.6
x = 0.4
x = 0.2
x = 0
La5/3MgTaO6
JCPDS : 01-076-3145
Intensity (a.u.)
10
20
30
40
50
60
2 θ (degree)
BaLaMgTaO6
(Cubic)
La5/3MgTaO6
(Monoclinic)
Intensity (a.u.)
30
31
32
33
2 θ (degree)

Fig. 2

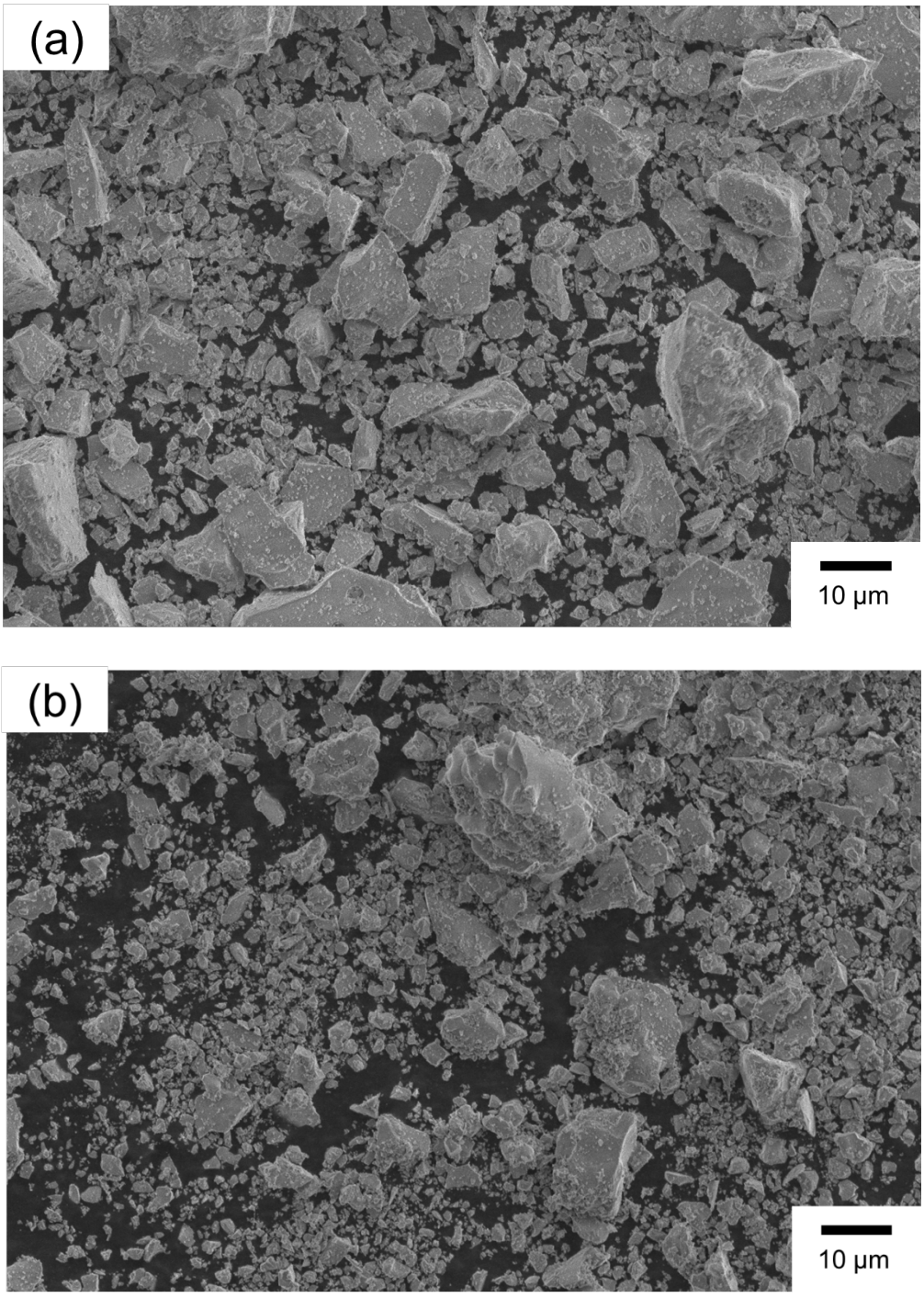

Fig. 3

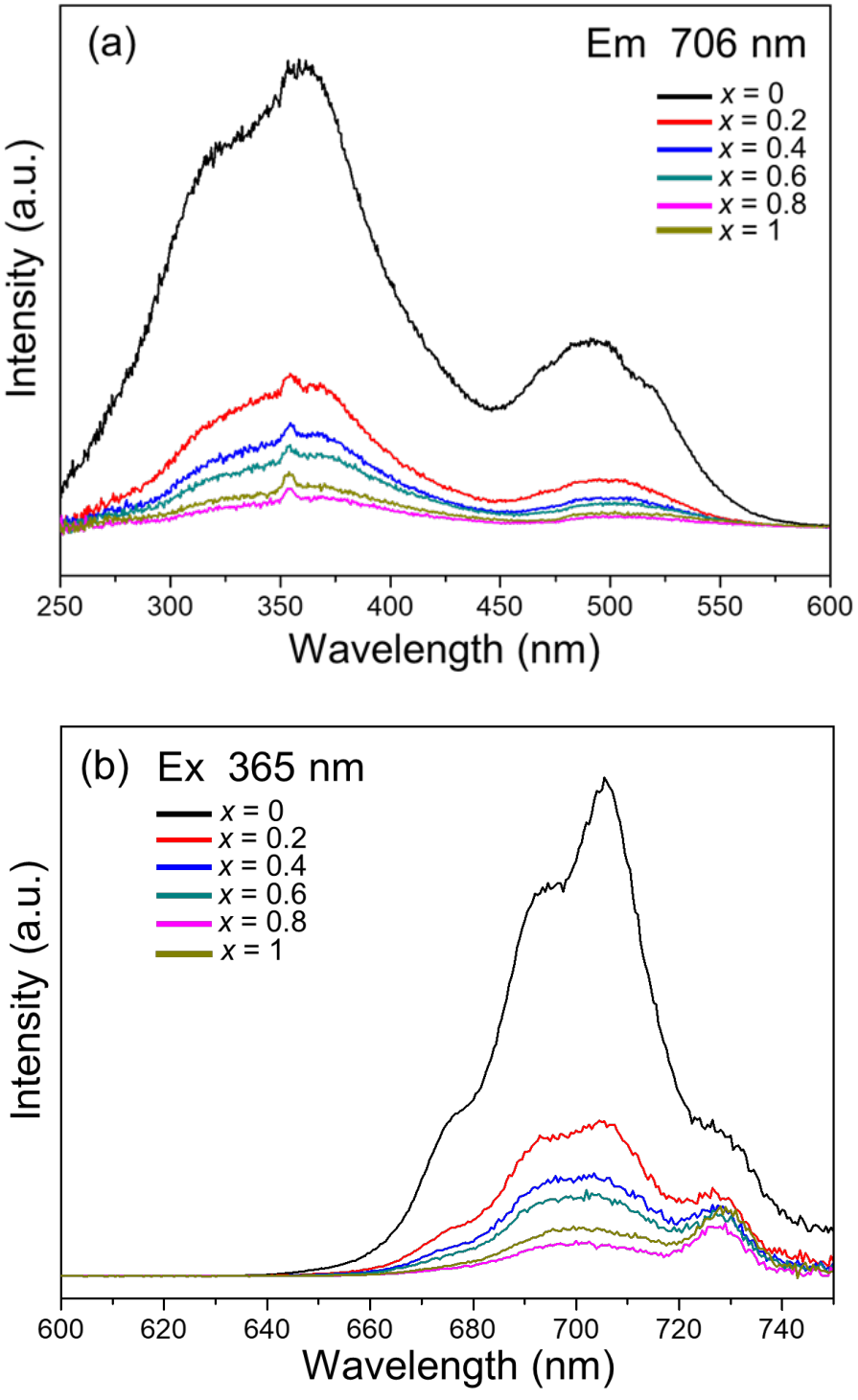
(a)
Em 706 nm
x = 0
x = 0.2
x = 0.4
x = 0.6
x = 0.8
x = 1
Intensity (a.u.)
250
300
350
400
450
500
550
600
Wavelength (nm)
(b) Ex 365 nm
x = 0
x = 0.2
x = 0.4
x = 0.6
x = 0.8
x = 1
Intensity (a.u.)
600
620
640
660
680
700
720
740
Wavelength (nm)

Fig. 4

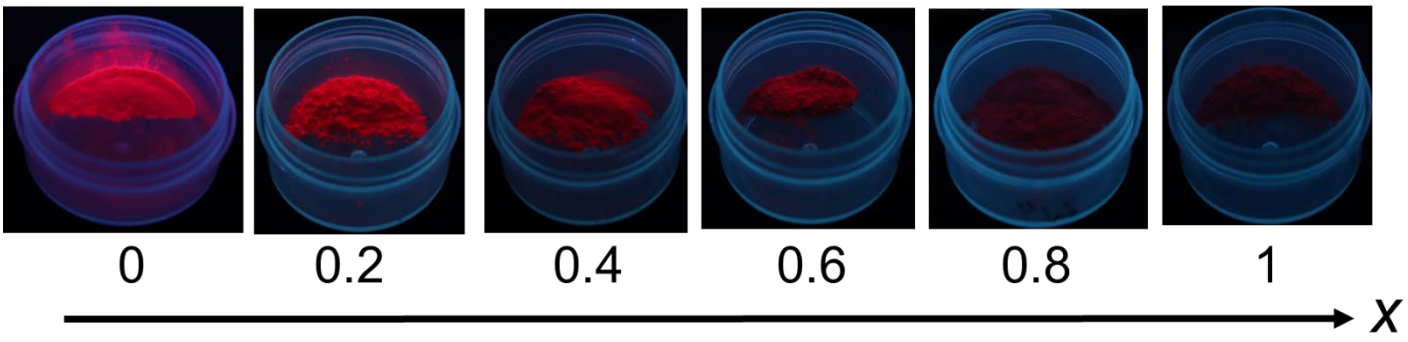

Fig. 5

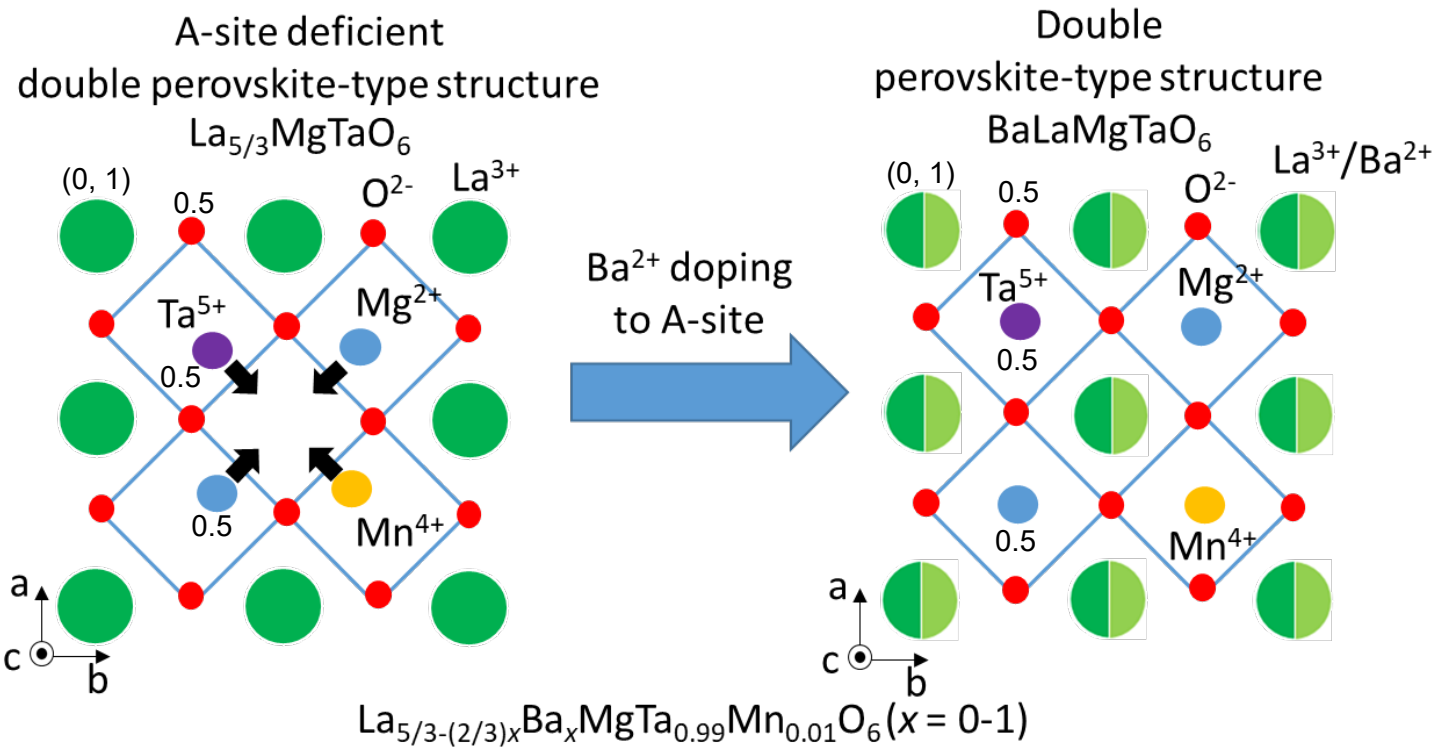
A-site deficient
double perovskite-type structure
$La_{5/3}MgTaO_6$
(0, 1)
0.5
O^{2-}
La^{3+}
Ta^{5+}
Mg^{2+}
0.5
0.5
Mn^{4+}
a
c
b
Ba^{2+} doping
to A-site
Double
perovskite-type structure
$BaLaMgTaO_6$
La^{3+}/Ba^{2+}
(0, 1)
0.5
O^{2-}
Ta^{5+}
Mg^{2+}
0.5
0.5
Mn^{4+}
a
c
b
$La_{5/3-(2/3)x}Ba_xMgTa_{0.99}Mn_{0.01}O_6$ (x = 0-1)

Fig. 6

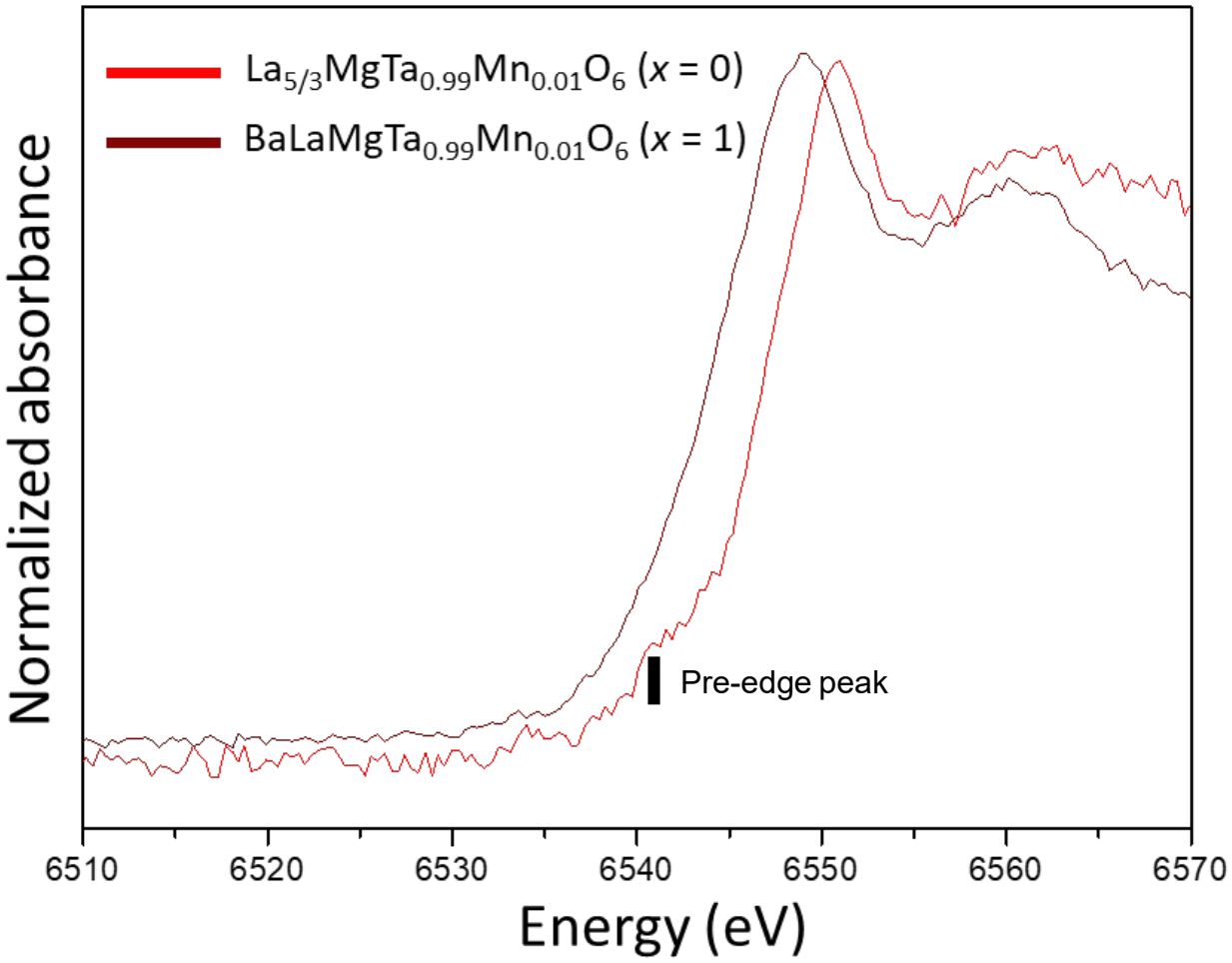
La5/3MgTa0.99Mn0.01O6 (x = 0)
BaLaMgTa0.99Mn0.01O6 (x = 1)
Pre-edge peak
Normalized absorbance
6510
6520
6530
6540
6550
6560
6570
Energy (eV)

Fig. 7

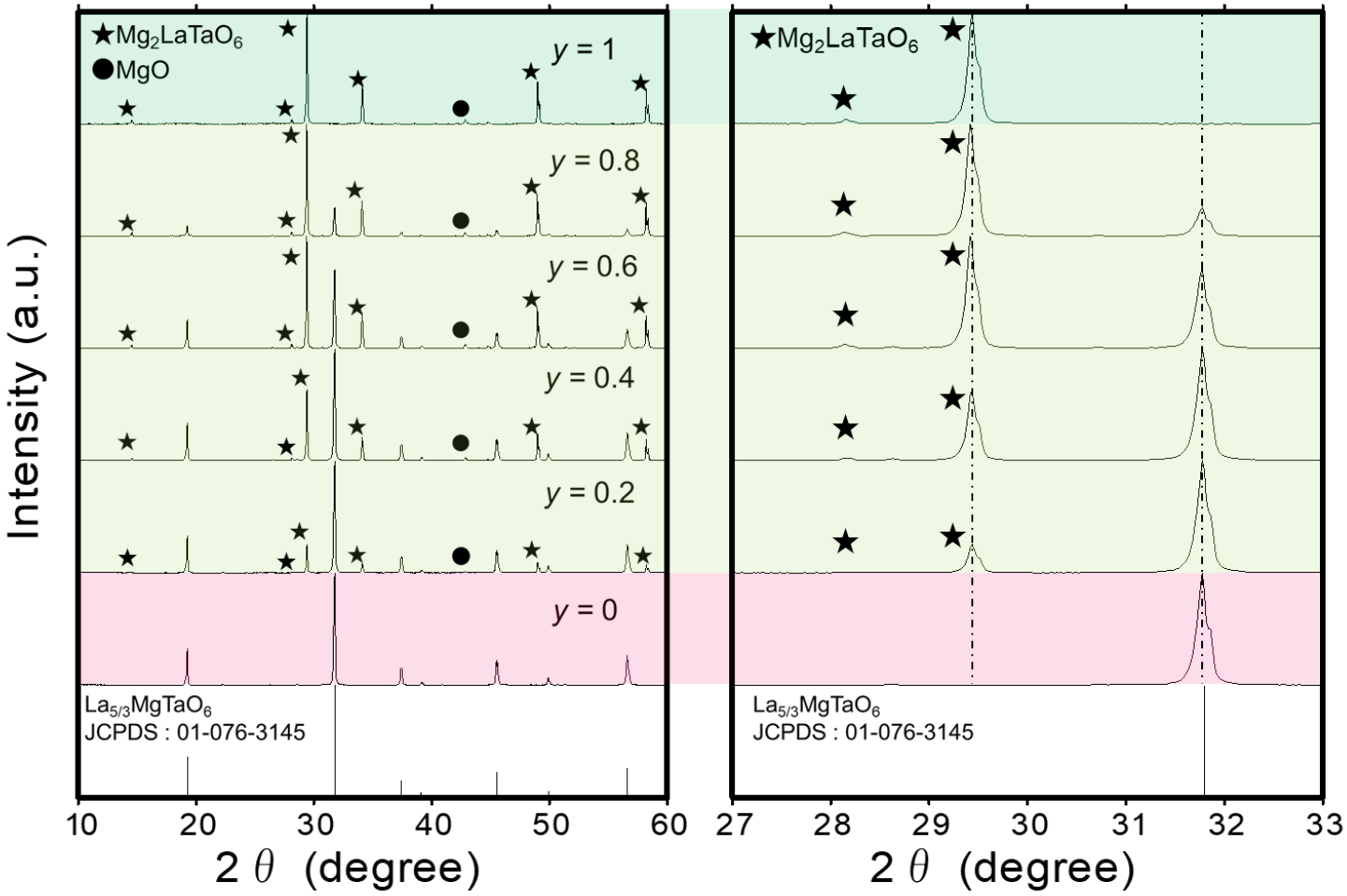
★Mg2LaTaO6
●MgO
y = 1
y = 0.8
y = 0.6
y = 0.4
y = 0.2
y = 0
La5/3MgTaO6
JCPDS : 01-076-3145
Intensity (a.u.)
10 20 30 40 50 60
2 θ (degree)
★Mg2LaTaO6
La5/3MgTaO6
JCPDS : 01-076-3145
27 28 29 30 31 32 33
2 θ (degree)

Fig. 8

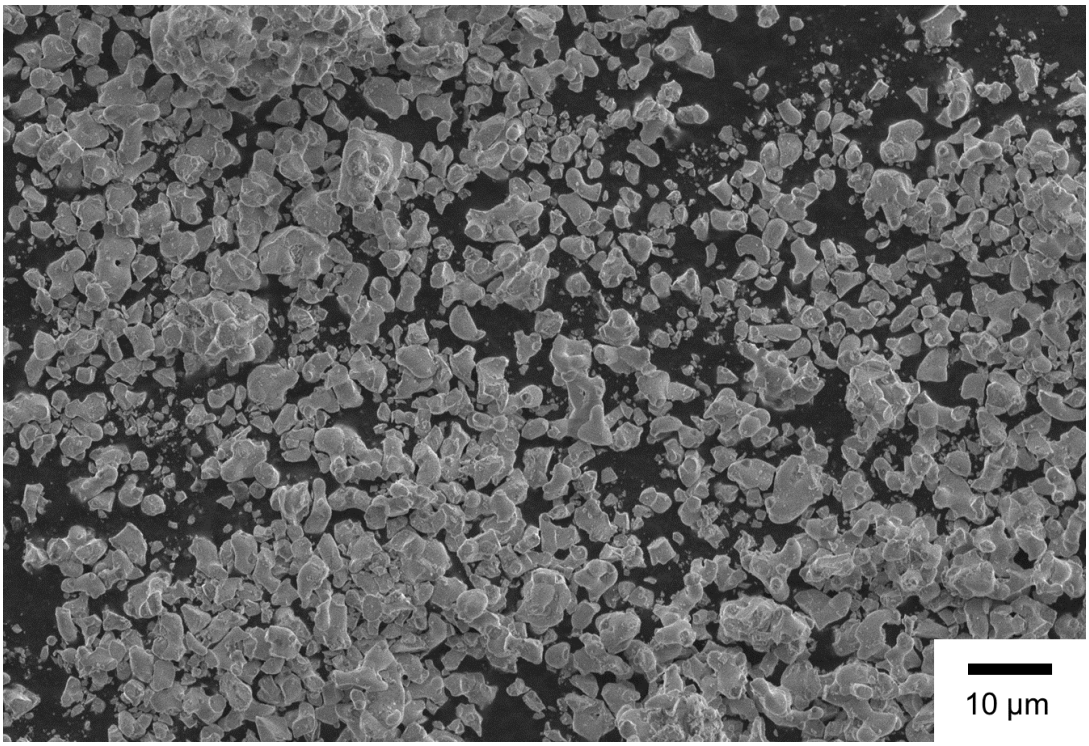

Fig. 9

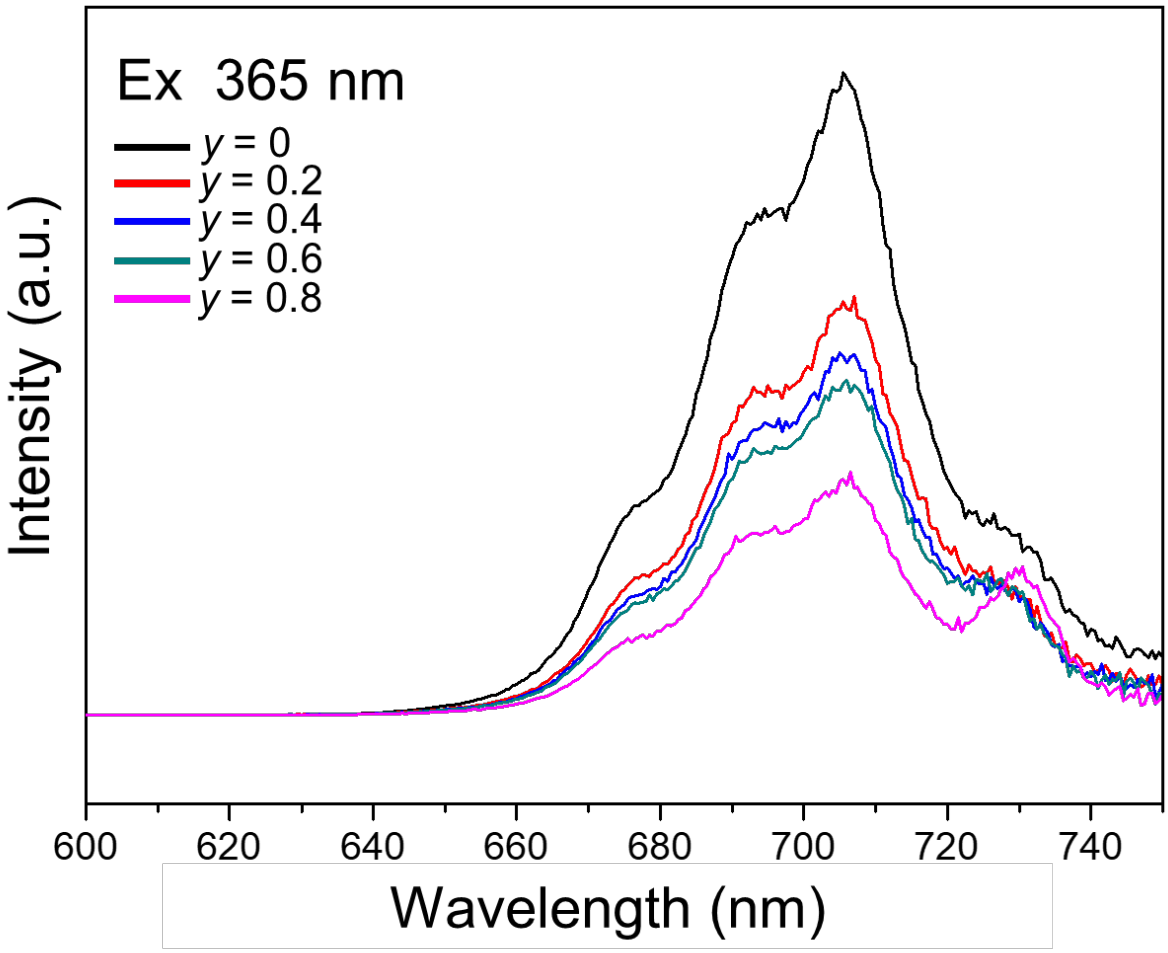
Ex 365 nm
y = 0
y = 0.2
y = 0.4
y = 0.6
y = 0.8
Intensity (a.u.)
600
620
640
660
680
700
720
740
Wavelength (nm)

Fig. 10

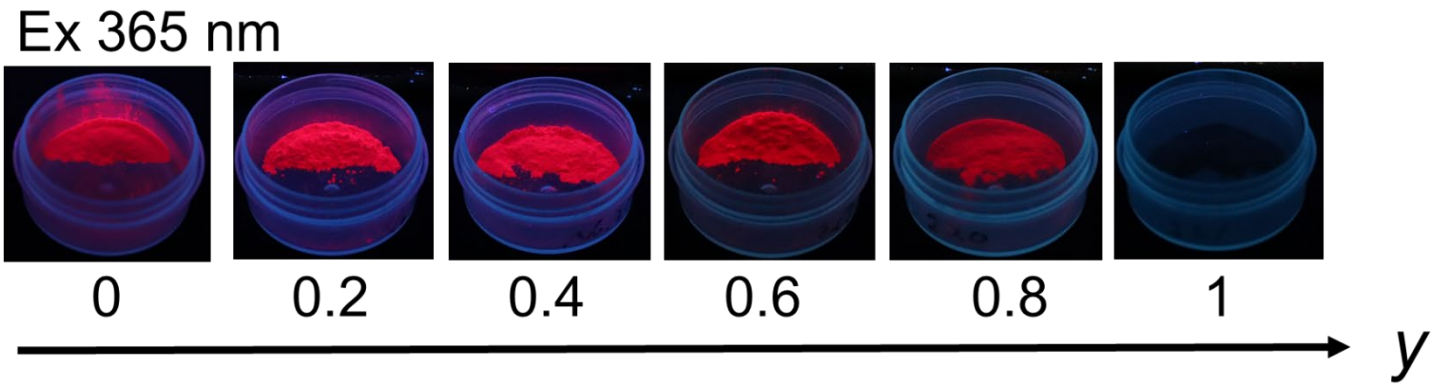

Fig. 11

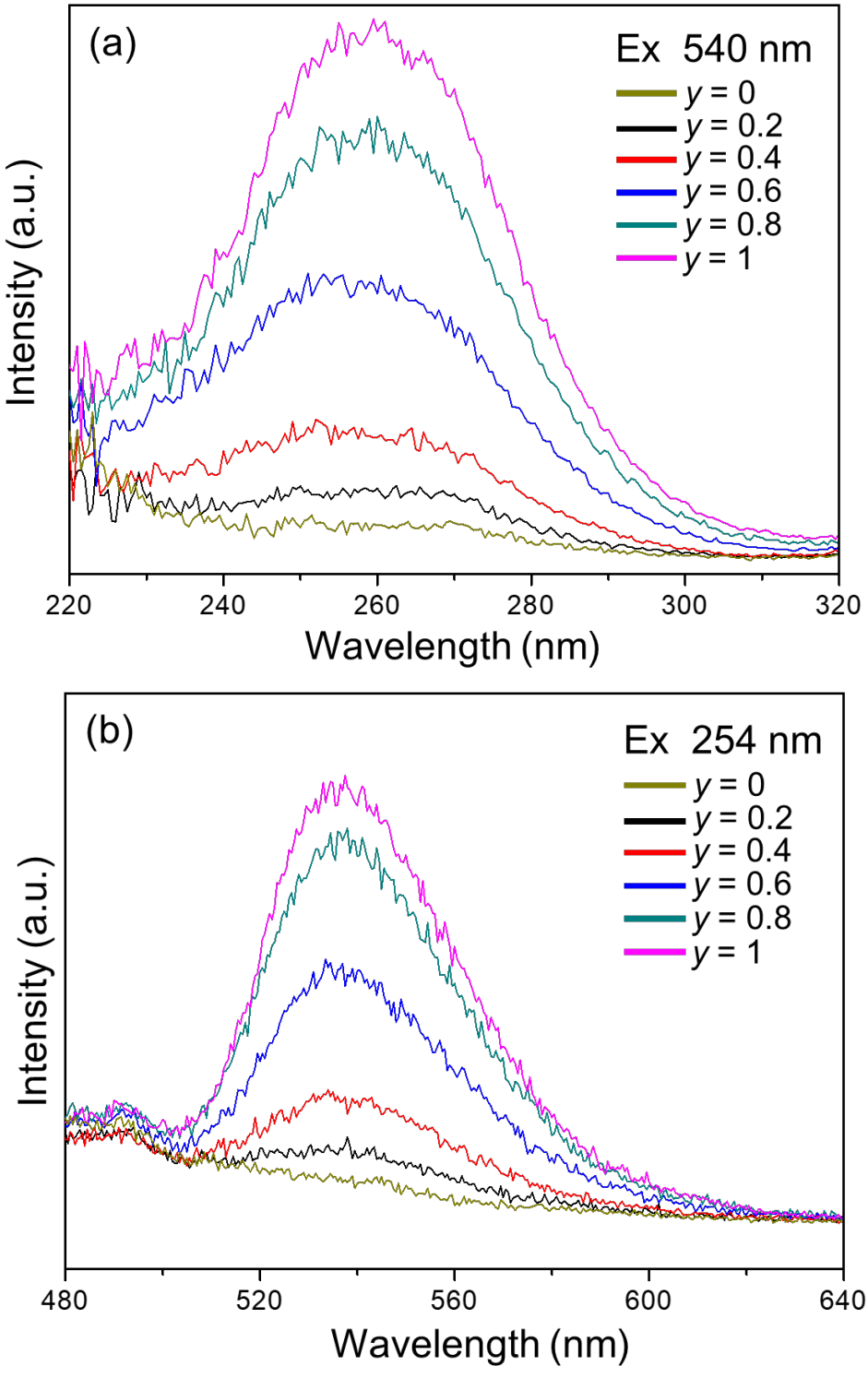
(a)
Ex 540 nm
y = 0
y = 0.2
y = 0.4
y = 0.6
y = 0.8
y = 1
Intensity (a.u.)
220
240
260
280
300
320
Wavelength (nm)
(b)
Ex 254 nm
y = 0
y = 0.2
y = 0.4
y = 0.6
y = 0.8
y = 1
Intensity (a.u.)
480
520
560
600
640
Wavelength (nm)

Fig. 12

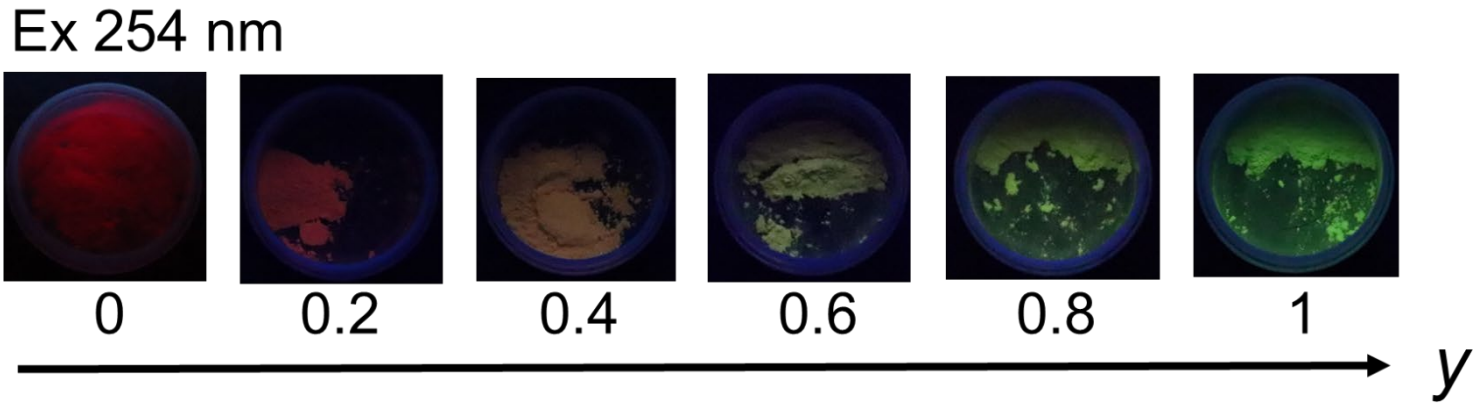

Fig. 13

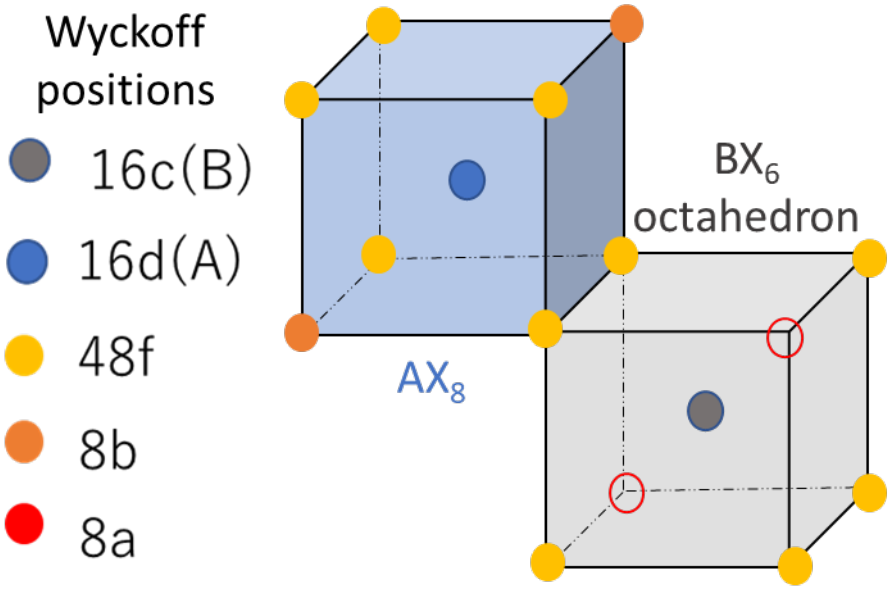

Fig. 14

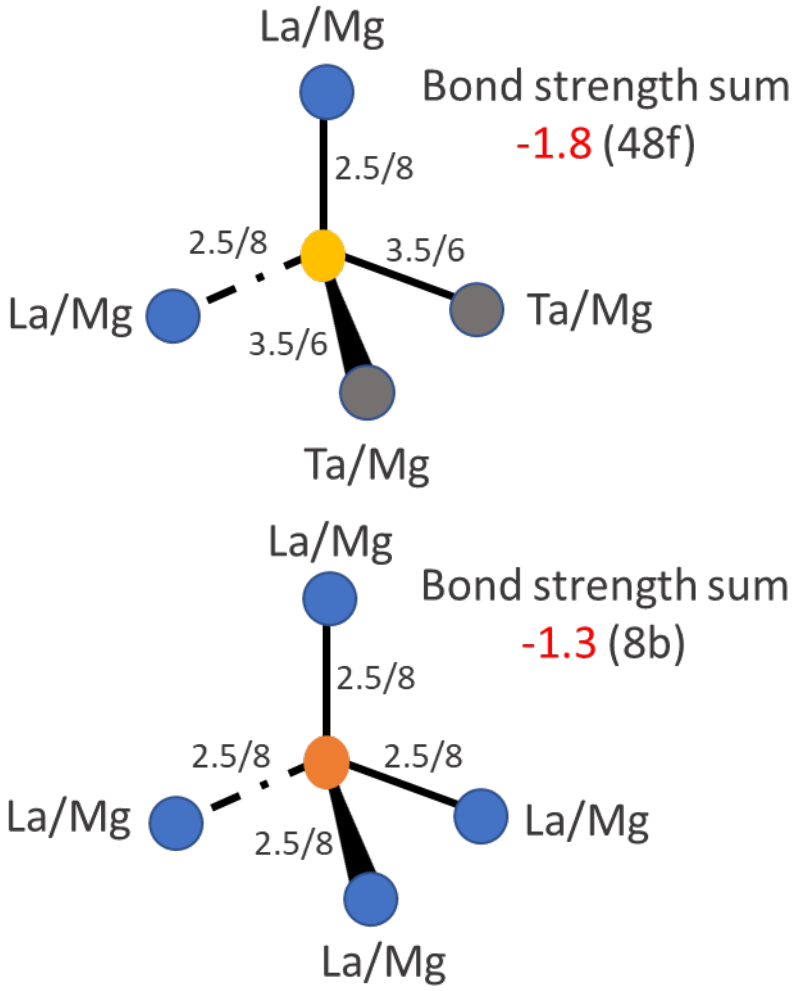

(Bond strength sum) = $-\sum_i \frac{V_i}{n_i}$

V_i : Valence of cation

n_i : Coordination number of cation

Fig. 15

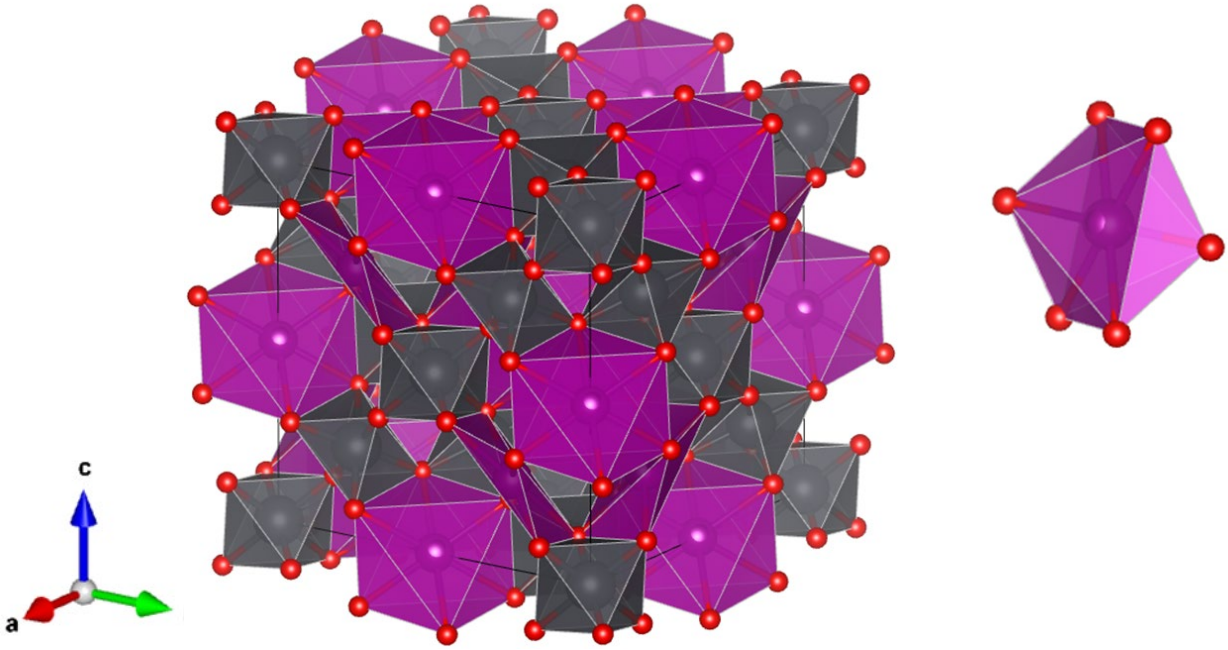

Fig. 16

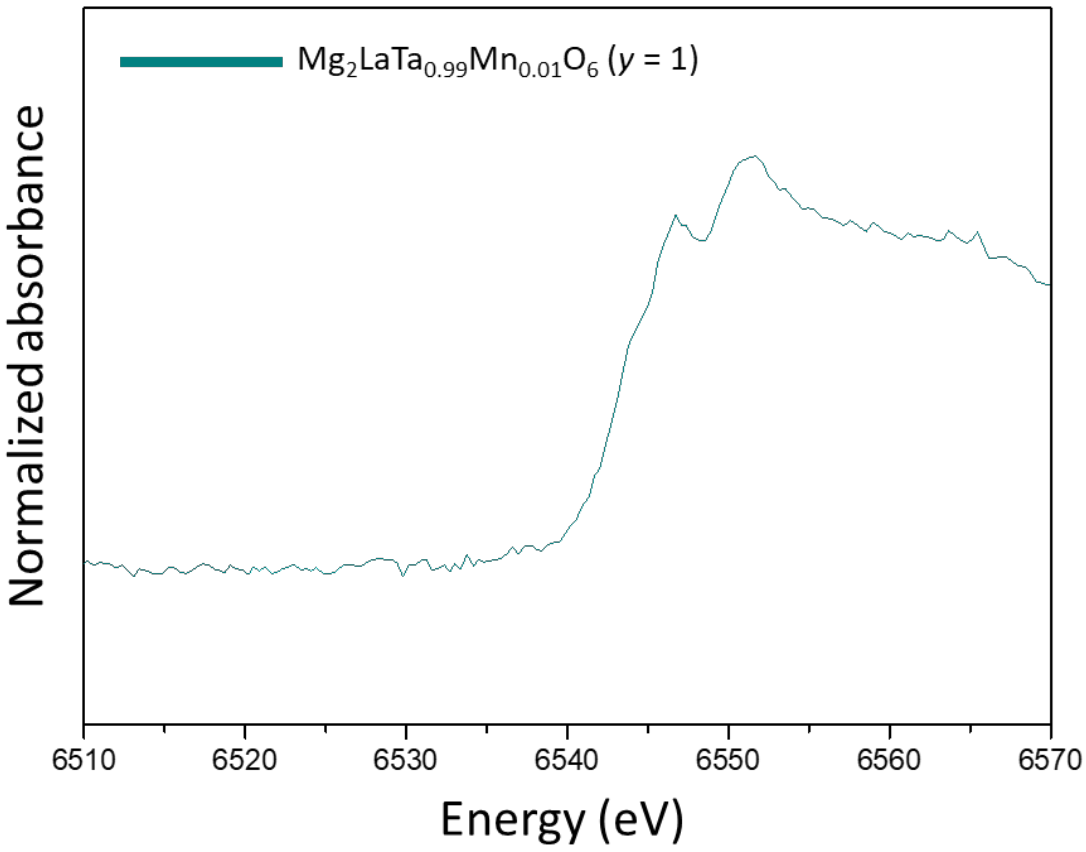
Mg2LaTa0.99Mn0.01O6 (y = 1)
Normalized absorbance
6510
6520
6530
6540
6550
6560
6570
Energy (eV)

Fig. 17

Table 1

Host	Coordination number	Emission wavelength (nm)	Ref.
$CdAl_2O_4$	4	495	[34]
$KAlSi_2O_6$	4	513	[36]
Na_2ZnSiO_4	4	515	[31]
$SrAl_2Si_2O_8$	4	517	[40]
Na_2MgGeO_4	4	521	[35]
Zn_2SnO_4	4	523	[33]
Zn_2SiO_4	4	530	[30]
Mg_2LaTaO_6	6	540	This study
$CdSiO_3$	6	575	[37]
$Na_2Mg_2Si_6O_{15}$	6	630	[39]
$KMgBO_3$	6	636	[32]
$MgGeO_3$	6	680	[38]